NANO LETTERS

Letter

Optimizing the Signal-to-Noise Ratio for Biosensing with Carbon Nanotube Transistors

Iddo Heller, Jaan Ma#nnik, Serge G. Lemay, and Cees Dekker

Nano Lett., **Article ASAP** • DOI: 10.1021/nl8031636

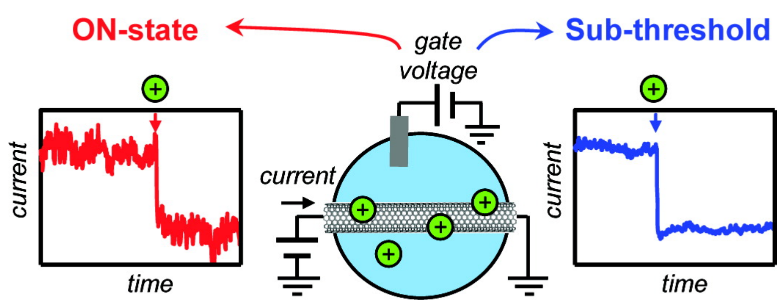

NANO LETTERS

XXXX
Vol. xx, No. x
-

Optimizing the Signal-to-Noise Ratio for Biosensing with Carbon Nanotube Transistors

Iddo Heller, Jaan Männik, Serge G. Lemay, and Cees Dekker*

Kavli Institute of Nanoscience, Delft University of Technology, Lorentzweg 1, 2628 CJ Delft, The Netherlands

Received October 18, 2008; Revised Manuscript Received December 2, 2008

ABSTRACT

The signal-to-noise ratio (SNR) for real-time biosensing with liquid-gated carbon nanotube transistors is crucial for exploring the limits of their sensitivity, but has not been studied thus far. Although biosensing is often performed at high transconductance where the device displays the largest gate response, here we show that the maximum SNR is actually obtained when the device is operated in the subthreshold regime. In the ON-state, additional contributions to the noise can lead to a reduction of the SNR by up to a factor of 5. For devices with passivated contact regions, the SNR in ON-state is even further reduced than for bare devices. We show that when the conductivity of the contact regions can be increased using a conventional back gate, the SNR in the ON-state can be improved. The results presented here demonstrate that biosensing experiments are best performed in the subthreshold regime for optimal SNR.

Single-walled carbon nanotubes[1] (SWNTs) employed in a field-effect-transistor layout[2] can be used as sensors for molecular adsorption.[3] The use of an electrolyte as a gate[4] that is in direct contact with the SWNT allows the gating efficiency to approach the theoretical upper limit (60 mV/decade),[5] indicating optimal sensitivity to the electrostatic environment. The combination of operation in aqueous solution, high sensitivity, and the unique one-dimensional geometry with a critical dimension in the size range of individual biomolecules makes carbon nanotubes outstanding biosensors.[6−9]

A next challenge in the use of nanotubes as biosensors is to push the sensitivity down to the lowest analyte concentrations[10,11] and ultimately down to single molecule sensitivity. In this context, optimizing the signal-to-noise ratio (SNR) is a crucial aspect, which has been given little attention to date. Previously, we discussed the dependence of the SNR for charge sensing on channel length.[12] In this report, we focus on the dependence of the SNR on gate potential and device architecture. To investigate the SNR, we study both the biosensing signal and the noise properties. The mechanism of biosensing with carbon nanotube transistors has been widely studied and is mostly attributed to electrostatic gating and Schottky-barrier modulation.[6,13] In a recent report, we found that transistors consisting of individual SWNTs are most reliably operated as contact-protected electrostatic charge sensors.[13] Here, we first show that the electrostatic gating effect of biomolecules is unaffected by contact protection, and that the real-time signal is highly dependent on the liquid gate. Interestingly, the sensor response can be enhanced by proper device precoating. Second, the low-frequency noise of carbon nanotube transistors, which exhibits a $1/f$-type spectrum,[14] reveals a strong gate-dependence,[12,15] consistent with a recently proposed charge-noise model.[12,16] Here we show that, in real-time SWNT-sensing experiments, the SNR is also gate-dependent. Finally, we study the origin of the dependence of the SNR on gate potential and device architecture, and we show that it can be related to fluctuations in the gate-independent device resistance.

SWNT transistors were fabricated on thermally oxidized Si wafers as described previously.[6] All devices consist of individually contacted semiconducting SWNTs. The devices are mounted in a home-built flow cell with access for a reference electrode. As depicted in Figure 1a a small V_{sd} voltage of 10 mV is applied over source and drain contacts to monitor device conductance while controlling the electrolyte potential, V_{lg}, using a reference electrode inserted in solution. An Ag/AgCl (3 M NaCl) standard reference electrode (BioAnalytical Systems) is used to avoid biosensing artifacts as described by Minot et al.[17] All aqueous solutions are buffered at pH 7 using phosphate buffer at millimolar concentrations. In this study two device layouts have been used. Figure 1a depicts the first layout, referred to as a bare device, where the entire length of the SWNT including the contact regions is exposed to solution. The liquid gate affects the doping level along the entire tube, as illustrated by the

* To whom correspondence should be addressed. E-mail: c.dekker@tudelft.nl.

10.1021/nl8031636 CCC: $40.75

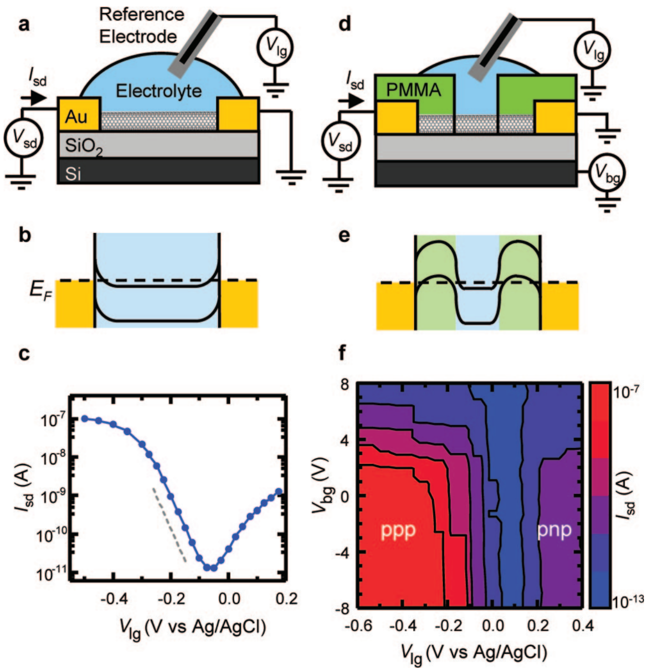

Figure 1. Gating of carbon nanotube transistors in two different device layouts. (a) Schematic device layout for a bare liquid-gated SWNT transistor. (b) Schematic band-structure (energy versus position) of an n-doped bare device. The dashed line indicates the energy of the Fermi level, E_F. The yellow sections on left and right sides indicate the occupied states on the Au contacts, whereas the blue section shows the conductance-band edge (top solid line) and valence-band edge (bottom solid line) of the liquid-gated carbon nanotube. (c) Experimental $I_{sd}-V_{lg}$ curve measured for a bare device. The dashed gray line indicates the ideal subthreshold slope of 60 mV/decade. (d) Schematic device layout for a contact-protected device (PMMA device). The contact regions are covered by a PMMA layer of approximately 600 nm thick, which limits the liquid-gated region to the central section of the nanotube. (e) Schematic band-structure of a pnp-doped PMMA device. The green sections indicate the band structure of the carbon nanotube covered by PMMA. (f) Plot of measured I_{sd} as a function of both V_{lg} and V_{bg} for a PMMA device. The color scale is logarithmic.

n-doped band structure in Figure 1b. A typical $I_{sd}-V_{lg}$ curve obtained from a bare device is shown in Figure 1c, revealing ambipolar conduction. The near-ideal gate coupling is illustrated by the slope in the subthreshold regime which approaches the ideal value of 60 mV/decade in the p-doped region (dashed line).[4] In the second device layout, depicted in Figure 1d, the contact regions and Au leads are insulated from solution by a layer of poly(methyl methacrylate) (PMMA).[18] This device layout is referred to as a PMMA device. As explained previously, the PMMA layer prevents work-function modulation at the contacts, yielding more reliable biosensors.[6] In addition, the PMMA layer significantly reduces the gate coupling to the PMMA-covered regions to a level comparable to the back gate. This is in contrast with the liquid-gated section, where the back-gate efficiency is negligible compared to that of the liquid gate. Now we can use both back gate and liquid gate to separately control the doping level of the different sections, as illustrated by the band structure of Figure 1e, which exhibits an intratube pnp-junction.[19] Figure 1f shows I_{sd} as a function of both V_{lg} and V_{bg} for a typical PMMA device. We note

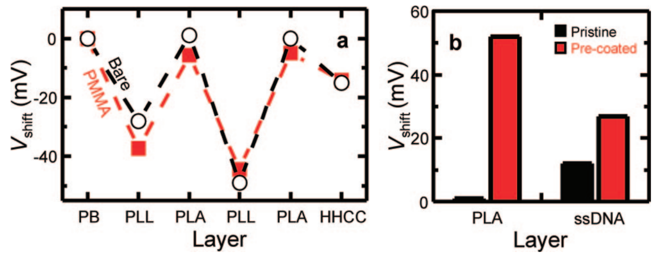

Figure 2. Electrostatic gating effect induced by biomolecule adsorption on liquid-gated SWNT-transistors. (a) V_{shift} of $I_{sd}-V_{lg}$ curves relative to the pristine condition (measured in phosphate buffer, PB) after subsequent adsorption of 200 nM poly L-lysine (PLL), 1 μM poly L-aspartic acid (PLA), 200 nM PLL, 1 μM PLA, and 1 μM horse-heart cytochrome-c (HHCC). The black and red curves were measured for a bare and PMMA device, respectively. (b) Comparison of V_{shift} for detection of either 1 μM PLA or 1 μM ssDNA (CATATTTCATGCGTTC) before (black columns) and after (red columns) device precoating with 200 nM PLL. The PLA adsorption experiment was performed on a different SWNT than the ssDNA adsorption experiment.

that at $V_{bg} = 0$ V, the device shows ambipolar conductance as a function of liquid-gate with a high ON-state p-conductance, indicating that the PMMA-covered section is naturally p-doped. In the following discussion, we will compare the biosensing signals and the low-frequency noise for these two device layouts to characterize the SNR.

We first study the biosensing signal, showing that the electrostatic gating effect of adsorbed biomolecules is comparable for the two different device layouts. In previous studies it has been shown that electrostatic gating by an adsorbed layer of charge on a SWNT transistor offsets the potential at the SWNT-liquid interface with respect to the value set by the reference electrode, thus shifting the $I_{sd}-V_{lg}$ curve along the voltage-axis.[6,20] Throughout this report we will focus on the electrostatic-gating mechanism of biosensing. As demonstrated previously, the electrostatic gating effect allows detection of subsequent adsorption of multiple layers of alternating charge.[20] In Figure 2a, we plot the liquid-gate-potential shift, V_{shift}, of the $I_{sd}-V_{lg}$ curves for a bare and a PMMA device during two subsequent adsorption cycles of poly-L-lysine (PLL) and poly-L-aspartic acid (PLA), followed by adsorption of horse heart cytochrome-c (HHCC). We observe that V_{shift} is directly comparable for both device layouts, even though the PMMA device has merely one-third of its SWNT length exposed to solution. This can be readily understood. The exposed section is in series with the PMMA-covered sections and dominates conductance in the subthreshold regime, where V_{shift} is determined. The shift can be approximated by $V_{shift} = q_{ads}/c_{dl}$, where c_{dl} is the double layer capacitance per unit length, and q_{ads} the adsorbed charge per unit length.[21] V_{shift} is thus independent of the exposed length of the SWNT.[22]

It is interesting to note that the magnitude of V_{shift} after addition of biomolecules strongly depends on the device pretreatment. Figure 2b shows that while addition of PLA has negligible effect on a pristine device, a ~50 mV shift upon PLA addition is observed after the device is coated with PLL. Similarly, an 11 mV shift due to adsorption of ssDNA on a pristine device can be enhanced to 25 mV if

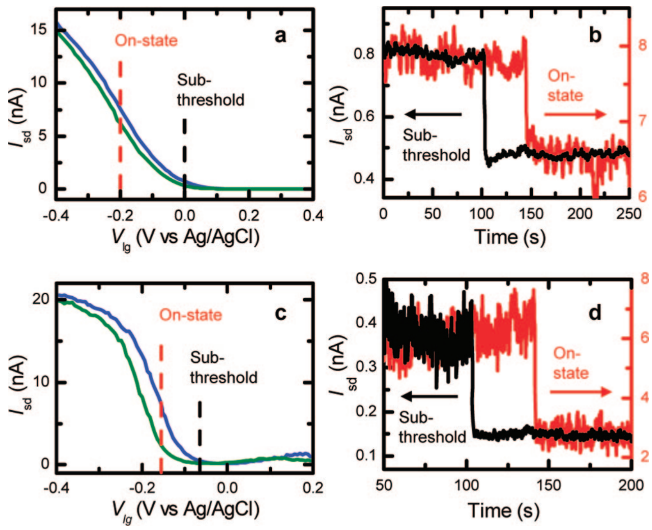

Figure 3. Signal-to-noise ratio enhancement in subthreshold regime. (a) $I_{sd}-V_{lg}$ curves recorded on a bare device in 10 mM KCl (blue) and 100 mM KCl (green) solutions. (b) Real-time current response to a step in the salt concentration (change from 10 to 100 mM KCl) at constant gate voltage of −200 (red) and 0 mV (black). (c) $I_{sd}-V_{lg}$ curves recorded on a PMMA-device in 1 μM PLA (blue) and in 200 nM PLL (green) solutions. (d) The corresponding real-time current changes upon changing from PLA to PLL at constant gate voltage of −150 (red) and −60 mV (black).

the device is coated with PLL. We attribute these enhancements to the changes in effective surface charge after precoating, which affect the electrostatic interaction between analyte and surface.

Next we turn to the SNR for electrostatic gating in real-time sensing experiments. We will show that the SNR is affected by the applied liquid-gate potential. Figure 3a shows $I_{sd}-V_{lg}$ curves recorded in electrolytes of different ionic strength. Similar to biomolecule adsorption, changing the salt concentration shifts the $I_{sd}-V_{lg}$ due to the electrostatic gating effect.[20] Since the change of salt concentration is reversible, we can repeat this experiment multiple times, allowing us to compare the real-time SNR when the device is operated at different values of V_{lg}. In Supporting Information Figure S1a,b, we show the $I_{sd}-V_{lg}$ curves of two subsequent cycles in which the salt concentration is changed from 10 mM KCl to 100 mM KCl, yielding equal values of $V_{shift} = 25$ mV. Figure 3b compares the two corresponding $I_{sd}(t)$ traces, recorded respectively near maximum slope dI_{sd}/dV_{lg} ($V_{lg} = -200$ mV, red curve) and toward subthreshold operation ($V_{lg} = 0$ mV, black curve). As can be seen in Figure 3b, the SNR is increased by about a factor of 3 in the subthreshold region compared to the SNR in the ON-state, even though ΔI_{sd} is about a factor of 5 smaller.

To illustrate a similar gate dependence of the SNR for biomolecule adsorption, we recorded time-traces acquired at different values of V_{lg} when changing from a PLA to a PLL solution. Figure 3c shows $I_{sd}-V_{lg}$ curves recorded before and after changing from a PLA to a PLL solution. Supporting Information Figure S1d shows the $I_{sd}-V_{lg}$ curves of a subsequent PLA-PLL adsorption experiment, revealing an equal $V_{shift} = 40$ mV for the two cycles. Figure 3d shows the corresponding time-traces recorded at $V_{lg} = -150$ mV (near maximum dI_{sd}/dV_{lg}, red trace) and at $V_{lg} = -60$ mV (in subthreshold regime, black trace). Although the black trace in Figure 3d shows a clear difference in noise level before and after biomolecule adsorption, the SNR in subthreshold regime is on average indeed better than in the ON-state. The large difference in noise level can be attributed to operation in the highly nonlinear subthreshold regime in combination with the relatively large shift, $V_{shift} = 40$ mV, upon biomolecule adsorption. The experiments of Figure 3 show qualitatively that, although it is intuitive to measure near the region of highest slope, dI_{sd}/dV_{lg}, measuring in subthreshold regime actually yields a better SNR.

In the following discussion, we will study the liquid-gate-potential dependence of the SNR in more detail by measuring both the signal and the low-frequency noise power as a function of liquid gate. As shown previously, the low-frequency noise of liquid-gated SWNT-transistors reveals a $1/f$-type spectrum, where the noise power is inversely proportional to the length, L, of the SWNT.[12,15,23] Figure 4a,b (reproduced from ref 12) plots I_{sd} and corresponding current noise-power spectral density at 1 Hz, S_I(1 Hz), as a function of V_{lg} for a bare device. Here the potential is indicated relative to the center of the band gap, V_{gap}. The source-drain current and noise spectra have been corrected for electrochemical currents that flow between the liquid gate and the drain, following procedures described previously.[12] Supporting Information Figure S5 presents a direct measurement of the electrochemical current (gate-drain current), which never exceeds 0.1 nA, and is typically in the order of 1 pA. Furthermore, the current between source and drain electrodes through solution is typically much smaller than 1 pA and is thus negligible in comparison to the current through the nanotube (cf. Supporting Information Figure S5). From the data in Figure 4a,b we can directly extract the gate dependence of the SNR: The signal, ΔI_{sd}, as a result of an electrostatic gating shift, V_{shift}, is to first approximation proportional to dI_{sd}/dV_{lg}, which we calculate from the $I_{sd}-V_{lg}$ curve. Note that for large V_{shift}, deviations from this approximation may occur due to nonlinearities in the $I_{sd}-V_{lg}$ curve. The low-frequency noise power in a biosensing experiment is proportional to the measured value of S_I(1 Hz), and thus the root-mean-square (rms) noise amplitude is proportional to $[S_I(1\ \mathrm{Hz})]^{1/2}$. In Figure 4e, we plot the length-normalized SNR for electrostatic sensing, defined as $SNR_L = |dI_{sd}/dV_{lg}|(S_I(1\ \mathrm{Hz})L)^{-1/2}$ for two bare devices (square symbols). As obvious from Figure 4e, the SNR_L for bare devices varies by up to a factor of 5 depending on gate potential, and peaks at the center of the band gap. The data for bare devices show that choosing optimal working conditions can lead to significant enhancement of the SNR.

Because we previously found that contact-protected devices provide a more reliable platform for biosensing,[13] it is important to also explore their signal and noise properties. We characterize the SNR of PMMA devices in Figure 4c−e. We will however limit our analysis to the p-region, since in the n-region an intratube pnp-junction is created. Transport through the device in n-region is then dominated by band-to-band tunneling at the interfaces between the liquid-gated

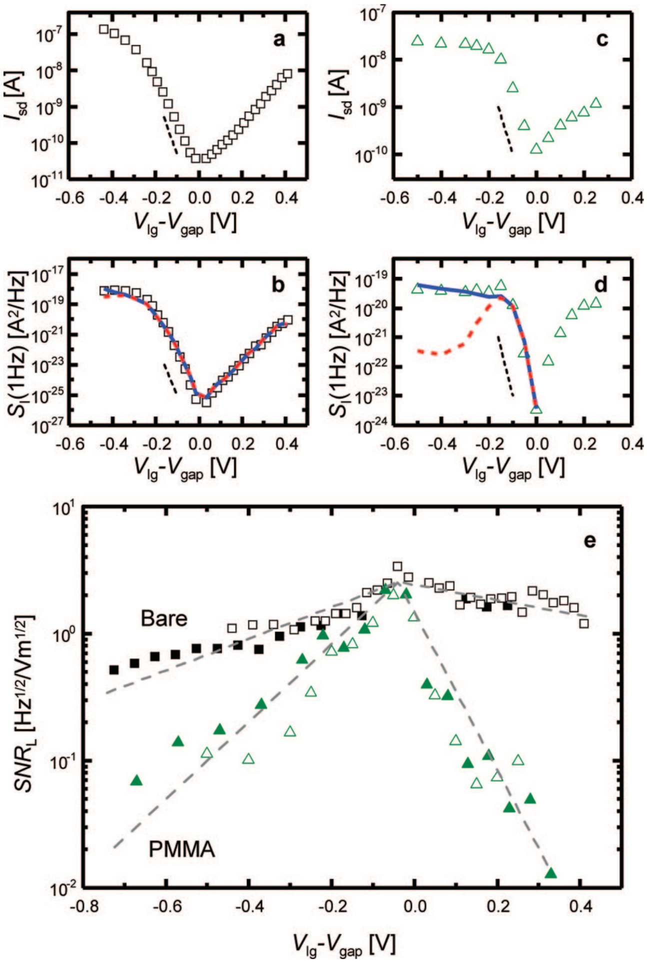

Figure 4. Comparison of the SNR for bare and PMMA devices. (a,b) I_{sd} and S_I(1 Hz) respectively for a bare device in 10 mM phosphate buffer. (c,d) I_{sd} and S_I(1 Hz) measured for a PMMA device. S_I (1 Hz) was obtained from $1/f$ fits to the low-frequency noise power spectra. Dashed black lines indicate the ideal subthreshold slopes of 60 mV/decade in $I_{sd}(V_{lg})$ (a,c) and 30 mV/decade in S_I (1 Hz) (b,d). Solid blue lines in (b,d) are fits to the augmented charge-noise model (defined in text), where the red dashed lines represent the contribution from the charge-noise component alone. (e) Length-normalized signal-to-noise ratio for charge sensing SNR_L (defined in text) for two bare devices (squares) and two PMMA devices (triangles), as calculated from the I_{sd} and S_I(1 Hz) data. The devices of panels a and c are represented by the open symbols, and the solid symbols are measured on two other devices. The dashed gray lines are guides to the eye to indicate the trends for bare devices and PMMA devices.

section and the PMMA-covered sections, which is expected to significantly change both the transport and noise characteristics. Figure 4c shows I_{sd} as a function of V_{lg} for a PMMA device. The corresponding S_I(1 Hz) is shown in Figure 4d. Finally, Figure 4e plots the SNR_L for two PMMA devices, where L was taken as the length of the liquid-gated section, again showing a maximum SNR in the subthreshold regime. The SNR_L however drops off by nearly 2 orders of magnitude toward the ON-state, a much larger decrease than observed for the bare devices. From Figure 4e we can conclude that the SNR_L for PMMA devices is optimal in the subthreshold regime, where it is equal to the SNR_L for bare devices.

To explain the origin of the observed gate-potential dependence of the SNR, we must consider the low-frequency noise characteristics in more detail. As recently shown by Tersoff,[16] the low-frequency noise is well described by an augmented charge-noise model, which predicts that $S_I(1\text{ Hz}) = S_{input}(dI_{sd}/dV_{lg})^2 + A_S(R_s/R_{tot})^2 I_{sd}^2$. Here the first term describes the effect of fluctuating charges in the vicinity of the SWNT that induce current noise through a field-effect. For this charge-noise component, $S_I(1\text{ Hz}) \propto S_{input}(dI_{sd}/dV_{lg})^2$, where S_{input} is a proportionality constant.[12] The second term describes additional gate-independent current-noise, which becomes apparent in ON-state and is modeled as a series resistor that exhibits low-frequency noise.[16] Here A_S represents the resistance-noise amplitude of this series resistor, and R_s and R_{tot} are the series resistance and total device resistance, respectively. The validity of this charge-noise model for liquid-gated SWNT-devices was recently confirmed by Männik et al.[12] The blue solid lines in Figure 4b,d represent two-parameter fits of S_{input} and α_R to the augmented charge-noise model, where $\alpha_R = A_S(R_S/V_{sd})^2$, using $A_S(R_s/R_{tot})^2 I_{sd}^2 = \alpha_R I_{sd}^4$. The augmented charge-noise model is in good agreement with the data for both bare and PMMA devices.

In Figure 4b,d, the contribution from the charge-noise component to the fit of the augmented charge-noise model is indicated by the red dashed lines. Interestingly, although the fit to the augmented charge-noise model is dominated by the charge-noise component in the subthreshold regime, in the ON-state the charge-noise component underestimates the current noise. This underestimation of the ON-state current noise is largest for the PMMA device (cf. Figure 4b,d) and correlates with the larger decrease of SNR_L in the ON-state for the PMMA devices. Furthermore, the rms noise amplitude of the charge-noise component is proportional $|dI_{sd}/dV_{lg}|$ and is thus proportional to the signal due to electrostatic gating. Consequently, if the current noise is described by the charge-noise component alone, SNR_L is predicted to be independent of V_{lg}. This is not what we observe experimentally for both bare and PMMA devices (cf. Figure 4e). The data in Figure 4 show that the decrease of SNR_L in the ON-state is directly correlated with the extent to which the charge-noise component underestimates the measured S_I.

We attribute the qualitative difference in the ON-state SNR between bare and PMMA devices to the presence of the weakly liquid-gate-coupled PMMA-covered sections. The PMMA device essentially acts as a liquid-gated SWNT transistor, composed of the central section that dominates transport and noise in subthreshold regime, in series with the PMMA-covered sections that can dominate transport and noise in the ON-state. This is confirmed by several observations: First, in the subthreshold regime, I_{sd} and S_I(1 Hz) show near-ideal slopes of 60 and 30 mV/decade, respectively,[24] directly comparable to bare devices (cf. black dashed lines in Figures 4a−d). Because the high subthreshold slopes indicate near-ideal gate coupling, which is only satisfied along the liquid-gated section of the PMMA device, we can conclude that in subthreshold regime both transport and noise properties are dominated by the liquid-gated section. Indeed, the peak value of the SNR, normalized to the length of the liquid-gated section only, is directly comparable to that of bare devices, indicating that the SNR in the subthreshold regime is also dominated by the liquid-gated section. In the ON-state however, the conductance of the PMMA-covered sections can significantly affect the total device conductance (cf. Figure 1e,f). Consequently, fluctuations in the conductance of these PMMA-covered sections will affect the total current noise in the ON-state. These conductance fluctuations are likely dominated by charge noise induced at the Schottky barriers of the metal-SWNT contacts, as described by Tersoff.[16] The conductance and noise related to the PMMA-covered sections is essentially constant over the range of liquid-gate potentials being probed due to the negligible liquid-gate-coupling of the PMMA-covered sections compared to the near-ideal liquid-gate-coupling of the exposed sections. Therefore, the current noise related to the PMMA-covered sections is included in the gate-independent series resistor term of the augmented charge-noise model, which dominates the current noise for PMMA devices in the ON-state (cf. Figure 4d). This additional noise related to the PMMA-covered sections can decrease the SNR, depending on how large the contribution of the series resistance is to the total device resistance.

In the final section of this report, we demonstrate how the SNR in ON-state for PMMA-devices can be improved. The model of the noise makes a clear prediction for improving the SNR of PMMA devices: Above, we suggested that the PMMA-covered regions affect the device SNR-characteristics depending on how large their contribution to the total device resistance is. Specifically in the ON-state, the PMMA-regions contribute the largest part of the device resistance, causing the overall device SNR to decrease in comparison to a bare device. This implies that the SNR in ON-state can be altered by changing the doping level of the PMMA-covered regions. As illustrated in Figure 1e,f, this can be accomplished using the back gate. Figure 5a−c show I_{sd}, S_I, and SNR, respectively, as a function of V_{lg} for a PMMA device measured at $V_{bg} = -8$ V (black), $V_{bg} = 0$ V (red), $V_{bg} = 4$ V (green), and $V_{bg} = 8$ V (blue). The I_{sd} and S_I data again show near-ideal subthreshold slopes. The curves measured at $V_{bg} = 8$ V (blue) however deviate, since the high resistivity of the PMMA-covered regions, gated into the band gap, now affects the device conductance over the entire V_{lg} range. The solid lines in Figure 5b are global fits to the augmented charge-noise model. Since one value of S_{input} was used to fit all four curves, the curves vary only in their value for α_R. The dashed lines represent the contribution from the charge-noise component only. As the back gate voltage increases the resistivity of the PMMA-covered regions, the contribution from the additional gate-independent noise becomes larger. A comparison of the ON-state noise with the noise measured when the device was completely covered by PMMA, as presented in Supporting Information Figure S2, indeed suggests that the ON-state noise can be attributed to the PMMA-covered sections. This behavior is directly reflected in the SNR curves as plotted in Figure 5c.

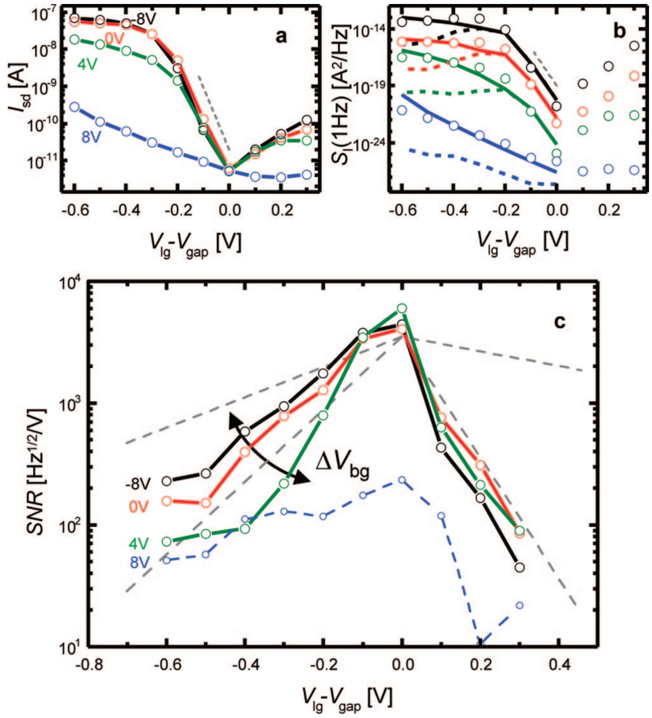

Figure 5. Effect of the back gate on the SNR for a PMMA device. (a) and (b) show respectively I_{sd} and S_I(1 Hz) data measured in 10 mM phosphate buffer at $V_{bg} = -8$ V (black), $V_{bg} = 0$ V (red), $V_{bg} = 4$ V (green), and $V_{bg} = 8$ V (blue). In (b) the S_I(1 Hz) tick labels correspond to the blue data set, the other data sets are subsequently offset by 2 orders of magnitude for clarity. Solid curves in panel b represent the augmented charge-noise model where the dashed curves represent the contribution by the charge-noise component alone. The 4 data sets were fitted using a common value for S_{input} but different values for α_R (see text). In panels a and b, the ideal subthreshold slopes of 60 and 30 mV/decade are indicated by gray dashed lines. (c) Shows the signal-to-noise ratio for charge sensing, SNR, corresponding to the curves in panels a and b. The dashed gray lines show the trends for bare and PMMA-devices corrected for length, as obtained from Figure 4e.

The gray dashed curves show the trends for bare and PMMA devices as previously found in Figure 4e. The maximum of SNR_L in the subthreshold regime is comparable to the previously presented devices, independent of the back-gate voltage. In the ON-state, the back gate allows varying the SNR up to 1 order of magnitude. At large negative back-gate voltage, the resistivity of the PMMA-covered regions, and thus their contribution to the noise, is suppressed, which allows the SNR to be partially recovered. The contribution from the PMMA-covered regions to the total device resistance is likely to be larger for large band gap devices than for small band gap devices. Therefore, we expect that the enhancement of the SNR at $V_{bg} = -8$ V with respect to the SNR at $V_{bg} = 0$ V is largest for large band gap devices. Indeed this is consistent with measurements on two other PMMA devices with band gaps of different size as presented in the Supporting Information Figures S3 and S4. The effect of the back gate on PMMA devices displayed in Figure 5 clearly illustrates the contribution of a noisy series resistor to the device's noise characteristics and its corresponding effect on the SNR.

In summary, we have studied the signal-to-noise ratio (SNR) for charge sensing with liquid-gated SWNT transistors and compared bare and contact-protected device layouts. We found that the SNR is gate-potential dependent and peaks at the center of the band gap. The SNR is lowest in the ON-state where additional contributions to the noise lead to a decrease in the SNR by up to a factor of 5 for bare devices. This effect is much more pronounced for contact-protected devices, which show a variation of the SNR over almost 2 orders of magnitude. For the PMMA devices, the back gate provides a handle to partially improve the SNR. Our findings indicate that for real-time adsorption experiments with SWNTs, the SNR is optimized when the device is operated in the subthreshold regime.

Acknowledgment. This work was supported by the Nederlandse Organisatie voor Wetenschappelijk Onderzoek (NWO) and NanoNed.

Supporting Information Available: Individually plotted $I_{sd}-V_{lg}$ curves for the experiments of Figure 3, comparison of ON-state noise of the device of Figure 5 in liquid-gated configuration with back-gated configuration at complete PMMA coverage, data of enhancement of ON-state SNR as measured for two additional PMMA devices with differently sized band gaps, a control experiment showing that the source-drain conductance through solution is negligible, and a photograph of the home-built flow cell. This material is available free of charge via the Internet at http://pubs.acs.org.

References

(1) Dekker, C. *Phys. Today* **1999**, *52*, 22–28.
(2) Tans, S. J.; Verschueren, A. R. M.; Dekker, C. *Nature* **1998**, *393*, 49–52.
(3) Kauffman, D. R.; Star, A. *Angew. Chem., Int. Ed.* **2008**, *47*, 6550–6570.
(4) Rosenblatt, S.; Yaish, Y.; Park, J.; Gore, J.; Sazonova, V.; McEuen, P. L. *Nano Lett.* **2002**, *2*, 869–872.
(5) Heller, I.; Kong, J.; Williams, K. A.; Dekker, C.; Lemay, S. G. *J. Am. Chem. Soc.* **2006**, *128*, 7353–7359.
(6) Kauffman, D. R.; Star, A. *Chem. Soc. Rev.* **2008**, *37*, 1197–1206.
(7) Allen, B. L.; Kichambare, P. D.; Star, A. *Adv. Mater.* **2007**, *19*, 1439–1451.
(8) Chen, R. J.; Bangsaruntip, S.; Drouvalakis, K. A.; Kam, N. W. S.; Shim, M.; Li, Y.; Kim, W.; Utz, P. J.; Dai, H. *Proc. Natl. Acad. Sci. U.S.A.* **2003**, *100*, 4984–4989.
(9) Besteman, K.; Lee, J. O.; Wiertz, F. G. M.; Heering, H. A.; Dekker, C. *Nano Lett.* **2003**, *3*, 727–730.
(10) Sheehan, P. E.; Whitman, L. J. *Nano Lett.* **2005**, *5*, 803–807.
(11) Squires, T. M.; Messinger, R. J.; Manalis, S. R. *Nat. Biotechnol.* **2008**, *26*, 417–426.
(12) Männik, J.; Heller, I.; Janssens, A. M.; Lemay, S. G.; Dekker, C. *Nano Lett.* **2008**, *8*, 685–688.
(13) Heller, I.; Janssens, A. M.; Männik, J.; Minot, E. D.; Lemay, S. G.; Dekker, C. *Nano Lett.* **2008**, *8*, 591–595.
(14) Collins, P. G.; Fuhrer, M. S.; Zettl, A. *Appl. Phys. Lett.* **2000**, *76*, 894.
(15) Briman, M.; Bradley, K.; Gruner, G. *J. Appl. Phys.* **2006**, *100*, 013505.
(16) Tersoff, J. *Nano Lett.* **2007**, *7*, 194.
(17) Minot, E. D.; Janssens, A. M.; Heller, I.; Heering, H. A.; Dekker, C.; Lemay, S. G. *Appl. Phys. Lett.* **2007**, *91*, 093507.
(18) Heller, I.; Kong, J.; Heering, H. A.; Williams, K. A.; Lemay, S. G.; Dekker, C. *Nano Lett.* **2005**, *5*, 137–142.
(19) Kong, J.; Cao, J.; Dai, H.; Anderson, E. *Appl. Phys. Lett.* **2002**, *80*, 73–75.
(20) Artyukhin, A. B.; Stadermann, M.; Friddle, R. W.; Stroeve, P.; Bakajin, O.; Noy, A. *Nano Lett.* **2006**, *6*, 2080–2085.
(21) Here we assume the quantum capacitance is negligible with respect to C_{dl}.
(22) Interestingly, the PMMA-covered sections have a small liquid-gate-dependence, and their transport characteristics can also be equally affected by an adsorbed layer of charge on the PMMA. In case the charge density on PMMA and SWNT is equal we expect that the $I-V_{lg}$ curve is shifted not only near the band gap, but over the entire V_{lg} range.
(23) Lin, Y. M.; Appenzeller, J.; Knoch, J.; Chen, Z. H.; Avouris, P. *Nano Lett.* **2006**, *6*, 930.
(24) In subthreshold, both I_{sd} and dI_{sd}/dV_{lg} decrease exponentially with 60 mV/decade. Correspondingly, if in subthreshold S_I is proportional to $(dI_{sd}/dV_{lg})^2$, S_I decreases with 30 mV/decade.

NL8031636